Structural basis underlying specific biochemical activities of non-muscle tropomyosin isoforms

Selvaraj, Muniyandi

2023-01-31

Selvaraj , M , Kokate , S B , Reggiano , G , Kogan , K , Kotila , T , Kremneva , E , DiMaio , F , Lappalainen , P & Huiskonen , J T 2023 , ' Structural basis underlying specific biochemical activities of non-muscle tropomyosin isoforms ' , Cell Reports , vol. 42 , no. 1 , 111900 . https://doi.org/10.1016/j.celre

http://hdl.handle.net/10138/355850
https://doi.org/10.1016/j.celrep.2022.111900

Cell Reports

Article

Structural basis underlying specific biochemical activities of non-muscle tropomyosin isoforms

Graphical abstract

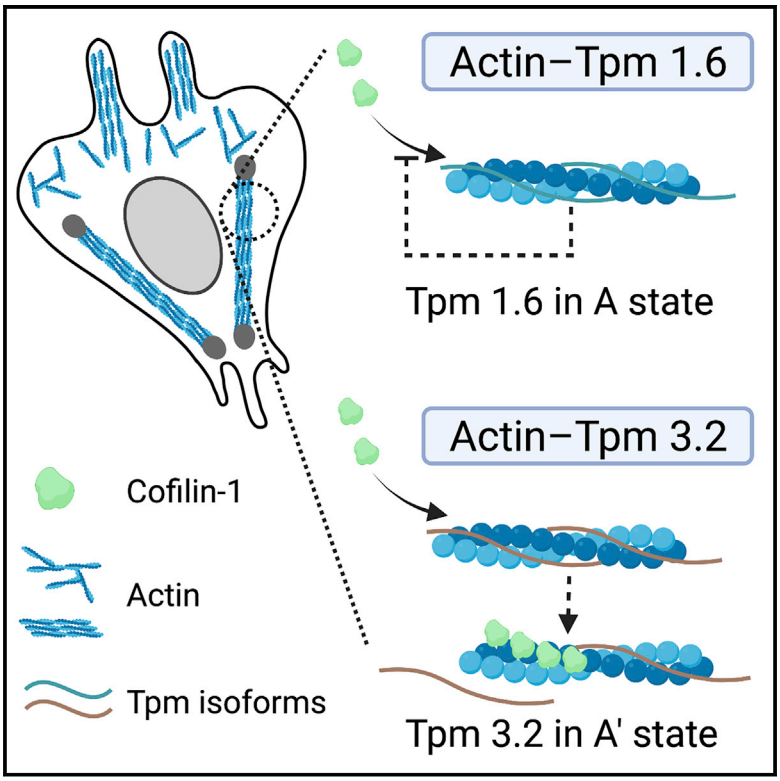

Highlights

- Non-muscle tropomyosins follow different “paths” along the actin filament
- Different positioning along actin prevents isoform mixing between Tpm1.6 and Tpm3.2
- Tpm1.6 inhibits cofilin binding to actin filaments due to a structural overlap

Authors

Muniyandi Selvaraj, Shrikant B. Kokate, Gabriella Reggiano, ..., Frank DiMaio, Pekka Lappalainen, Juha T. Huiskonen

Correspondence

pekka.lappalainen@helsinki.fi (P.L.), juha.huiskonen@helsinki.fi (J.T.H.)

In brief

Selvaraj et al. report the cryo-EM structures of non-muscle tropomyosins, which are central actin-binding proteins regulating the organization and dynamics of cellular actin filament arrays. The study elucidates the molecular basis underlying specific functions and sub-cellular localizations of functionally distinct tropomyosin isoforms in non-muscle cells.

Selvaraj et al., 2023, Cell Reports *42*, 111900
January 31, 2023
https://doi.org/10.1016/j.celrep.2022.111900

CellPress

Cell Reports

CellPress
OPEN ACCESS

Article

Structural basis underlying specific biochemical activities of non-muscle tropomyosin isoforms

Muniyandi Selvaraj,[1,3,4] Shrikant B. Kokate,[1,4] Gabriella Reggiano,[2] Konstantin Kogan,[1] Tommi Kotila,[1] Elena Kremneva,[1] Frank DiMaio,[2] Pekka Lappalainen,[1,5,*] and Juha T. Huiskonen[1,*]

[1]Institute of Biotechnology, Helsinki Institute of Life Science HiLIFE, University of Helsinki, P.O. Box 56, 00014 Helsinki, Finland
[2]Department of Biochemistry, University of Washington, Seattle, WA 98195, USA
[3]Present address: The Sainsbury Laboratory, Norwich Research Park, Norwich NR4 7UH, UK
[4]These authors contributed equally
[5]Lead contact
*Correspondence: pekka.lappalainen@helsinki.fi (P.L.), juha.huiskonen@helsinki.fi (J.T.H.)
https://doi.org/10.1016/j.celrep.2022.111900

SUMMARY

The actin cytoskeleton is critical for cell migration, morphogenesis, endocytosis, organelle dynamics, and cytokinesis. To support diverse cellular processes, actin filaments form a variety of structures with specific architectures and dynamic properties. Key proteins specifying actin filaments are tropomyosins. Non-muscle cells express several functionally non-redundant tropomyosin isoforms, which differentially control the interactions of other proteins, including myosins and ADF/cofilin, with actin filaments. However, the underlying molecular mechanisms have remained elusive. By determining the cryogenic electron microscopy structures of actin filaments decorated by two functionally distinct non-muscle tropomyosin isoforms, Tpm1.6 and Tpm3.2, we reveal that actin filament conformation remains unaffected upon binding. However, Tpm1.6 and Tpm3.2 follow different paths along the actin filament major groove, providing an explanation for their incapability to co-polymerize on actin filaments. We also elucidate the molecular basis underlying specific roles of Tpm1.6 and Tpm3.2 in myosin II activation and protecting actin filaments from ADF/cofilin-catalyzed severing.

INTRODUCTION

The actin cytoskeleton is critical for various cellular processes such as morphogenesis, motility, endocytosis, mechanosensing, and cytokinesis. To fulfill the specific needs of these diverse cellular processes, actin filaments assemble into a variety of structures with different architectures and dynamic properties and produce force through coordinated filament polymerization, as well as by serving as tracks for myosin motor proteins. Actin filaments of the different cytoskeletal structures associate with specific sets of actin-binding proteins, which give rise to distinct properties of actin filaments.[1,2] In plants, the functional variety of actin filament structures has been proposed to derive from the presence of a large number of closely related actin isoforms.[3] In contrast, fungi and metazoan cells express only one or few actin isoforms, so the functionally different actin filament structures in these organisms rely on proteins interacting with actin. These include tropomyosins (Tpms), which are elongated α-helical dimers that form head-to-tail oligomers along actin filaments. Tpms control the interactions of other proteins with actin filaments and regulate the stability of the actin filaments.[4]

The functions of Tpms have been studied extensively in striated muscles. Tpms, together with a heteromeric protein complex consisting of troponin T, troponin I, and troponin C, control the association of myosin motor II domains of thick filaments with thin actin filaments in a Ca^{2+}-dependent manner.[5] Recent cryogenic electron microscopy (cryo-EM) structures shed light on the mechanisms by which muscle Tpms (Tpm1.1 homodimer or Tmp1.1/Tpm2.2. heterodimers) interact with muscle actin filaments, and how the Tpm-troponin complex controls association of myosin II motor domains with actin filaments in muscle sarcomeres.[6–10] In an inactive Ca^{2+}-free state (also referred to as blocked or "B-state"), the troponin complex stabilizes Tpm on an actin filament in a position that hinders myosin motor domain interaction. In the presence of Ca^{2+}, the troponin complex undergoes a conformational change, which shifts the Tpm oligomer within the major groove of the actin filament by ~10 Å to the "C-state," where the myosin-binding site is partially uncovered.[9] Myosin binding to the actin filament further moves Tpm to an otherwise energetically unfavorable "M-state" position on an actin filament, resulting in actin-mediated activation of the myosin ATPase.[6,8,10] In the absence of troponin complex and other proteins (apo or "A-state"), Tpm binds to an intermediate position between the B- and C-states that overlaps with the myosin-binding site.[7]

Tpms play important roles also in non-muscle cells where they can activate myosins similarly to striated muscles, as well as inhibit actin-interactions of other proteins such as ADF/cofilin and fimbrin.[11–13] Consequently, in animal non-muscle cells, Tpms are critical for the maintenance and function of actomyosin

structures.[14,15] A large number (>40) of different Tpm isoforms can be generated through alternative splicing from four *TPM* genes in mammals, and several different Tpm isoforms are typically co-expressed in non-muscle cells.[16] Depending on their length, these proteins can be classified into high- and low-molecular-weight Tpms. Different non-muscle Tpm isoforms typically display at least partially non-overlapping localization patterns in cells and are functionally non-redundant with each other.[14,16–21] Moreover, biochemical studies on a subset of the most abundant non-muscle Tpm isoforms revealed that they differentially affect ADF/cofilin-mediated actin filament disassembly and activation of non-muscle myosin II. For example, Tpm1.6 and Tpm1.7 inhibit ADF/cofilin-catalyzed actin filament severing but do not activate myosin II. On the other hand, Tpm3.1, Tpm3.2, and Tpm4.2 do not efficiently protect actin filaments from ADF/cofilin but increase the non-muscle myosin II steady-state ATPase rate.[22–24] Despite the importance of different Tpm isoforms in specifying functionally distinct actin filaments in non-muscle cells, the underlying molecular mechanisms remain elusive.

The functional differences between non-muscle Tpms may arise from their different effects on the conformation of the actin filament they interact with, or from differences in their binding sites along the actin filament. The distinct functions could also be, at least partially, due to differences in the amino acid sequences of Tpms that could modulate the binding of other proteins on Tpm-decorated actin filaments. To address these different hypotheses, we focused here on two functionally distinct members of the family, Tpm1.6 and Tpm3.2. Of these two, Tpm1.6 exhibits a very slow off-rate from actin filaments and protects filaments from ADF/cofilin-catalyzed severing but does not activate non-muscle myosin II. Tpm3.2, on the other hand, displays rapid dynamics on actin filaments and accelerates the steady-state ATPase rate of non-muscle myosin II in the presence of actin filaments, but it does not efficiently protect actin filaments from ADF/cofilin.[22] By determining the cryo-EM structures of β/γ-actin filaments decorated either by Tpm1.6 or by Tpm3.2, we revealed that the conformation of the actin filament remains unaffected. However, the two non-muscle Tpm isoforms follow slightly different paths along the major groove of the actin filament. Molecular modeling provides a plausible explanation for the incapability of these two Tpm isoforms to co-polymerize with each other on actin filaments and for their different effects on myosin II and ADF/cofilins. This is further corroborated by our biochemical assays. Taken together, our results shed light on the specific biochemical activities of non-muscle Tpms.

RESULTS

Structures of β/γ-actin filaments decorated with non-muscle tropomyosins

To determine the molecular architecture of functionally distinct non-muscle actin-tropomyosin complexes, we expressed and purified Tpm1.6 and Tpm3.2 isoforms. Tpm1.6 is a high-molecular-weight Tpm (284 residues) generated from the *TPM1* gene, whereas Tpm3.2 is a low-molecular-weight Tpm (248 residues) generated from the *TPM3* gene. The two isoforms display high amino acid sequence conservation in their central regions but differ especially in the regions adjacent to their ends (Figure S1). We performed cryo-EM imaging on reconstituted complexes of both Tpm1.6 and 3.2 with β/γ-actin filaments. Our initial attempts to image the complexes revealed only bare actin, although either Tpm1.6 or Tpm3.2 had been added in excess. However, replacing NaCl in the sample buffer with sodium acetate (see STAR Methods), as previously done in studies on muscle actin:Tpm:-myosin complexes,[8] resulted in a good decoration of actin filaments by both non-muscle Tpms.

Using a single-particle-based helical reconstruction approach,[25] we reconstructed the 3D structure of the actin:Tpm1.6 complex at an average resolution of 3.9 Å (Figures 1A, 1B, and S2; Table S1). The filament measures approximately 90 Å in diameter (Figure 1A). Actin was well-resolved, allowing atomic model building. The Tpm1.6 density was ordered sufficiently to separate the coiled-coils formed by the two α-helices in the Tpm1.6 dimer (Figures 1A and 1B). However, the symmetry mismatch in the actin:Tpm1.6 assemblies, owing to the binding of one Tpm molecule per several actin monomers, hampered resolving the side chains of Tpm1.6 amino acid residues in the averaged density.[7] Furthermore, the backbones of Tpm1.6 α-helices in the coiled-coil were unresolved, suggesting that the turn of the α-helix is not in phase with the symmetry of the actin filament, resulting in incoherent averaging of the Tpm1.6 backbone. Notably, the binding of Tpm1.6 left the structure of the actin filament unaltered; the refined helical symmetry parameters of actin:Tpm1.6 (rise 27.8 Å; turn −166.5°) were nearly identical to those of bare chicken muscle actin (27.5 Å, −166.6°) reported earlier.[26]

To compare the binding of Tpm3.2 and Tpm1.6 to actin filaments, we also determined the structure of actin:Tpm3.2 complex to 4.6-Å resolution, using the same method as above (Figures 1C and S3; Table S1). A comparison of the Tpm densities relative to actin in these two complexes showed that the Tpm1.6 and Tpm3.2 dimers bind on different tracks on the surface of the actin filament (Figures 1B and 1C). In both complexes, the Tpm binds to the major groove region of actin involving actin subdomains 1, 3, and 4, but excluding residues of actin subdomain 2 (Figures 1D and 1E). However, the position of Tpm3.2 is shifted slightly (~5 Å) toward subdomains 3 and 4 when compared with the position of Tpm1.6 (Figure 1F). The root-mean-square deviation was 1.02 Å for Tpm1.6-decorated actin (between 364 Cα-atom positions) and 1.08 Å for Tpm3.2-decorated actin (between 365 Cα-atom positions) when compared with bare actin (PDB: 6DJO),[26] indicating that all three actin structures have a highly similar conformation. The helical parameters of Tpm3.2-decorated actin (rise 27.8 Å, turn −166.4°) were also nearly identical to those of bare actin. Together, these structures reveal that the two functionally distinct non-muscle Tpm isoforms leave the conformation of the actin filament unaffected but follow slightly different paths along the major groove of the actin filament.

Two non-muscle tropomyosin isoforms bind actin via analogous salt bridges

In the absence of cryo-EM density for tropomyosin side chains, we turned to atomistic modeling using Rosetta to study the detailed interactions of Tpm1.6 and Tpm3.2 with actin filaments.

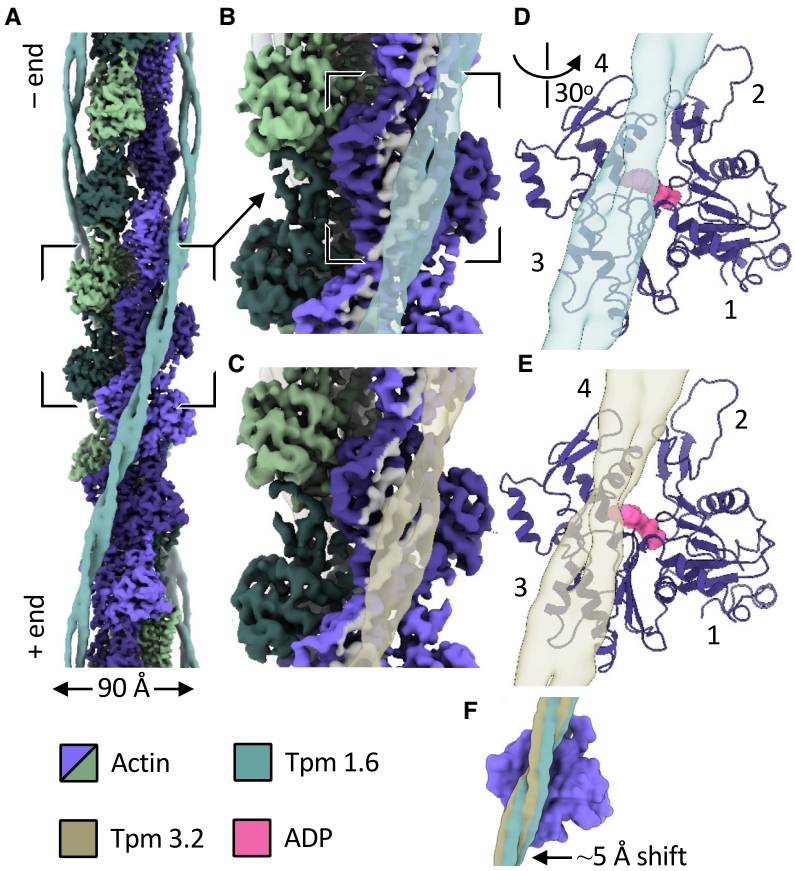

Figure 1. Cryo-EM structures of actin/non-muscle tropomyosin complexes

(A) Cryo-EM density of actin:Tpm1.6 complex is shown. Actin plus (barbed) and minus (pointed) ends are labeled. The density has been segmented, and actin subunits are colored individually. The Tpm1.6 density has been filtered to 7-Å resolution.

(B) A close-up of the area indicated in (A) is shown. Tmp1.6 density is shown as a transparent surface. Those parts of the actin surface that reside at 10 Å distance or closer to the Tpm1.6 have been colored in gray.

(C) The same view as in (B) is shown for actin:Tpm3.2 complex.

(D) A close-up of the area highlighted in (B) is shown rotated as indicated. The actin model is shown as a ribbon, the ADP model is shown as a surface, and the Tpm1.6 density as a transparent surface. The different subdomains of actin are labeled 1–4.

(E) The same view as in (D) is shown for actin Tpm3.2 complex.

(F) Tpm3.2 is shifted slightly (5 Å) in its position relative to the Tpm1.6 density. The actin atomic model from (D) is shown as a surface.

See also Figures S1–S3.

We modeled the two Tpms as coiled-coils by combining AlphaFold with Rosetta-based energy minimization using the cryo-EM density maps. The interfaces generated by Alphafold were verified by Rosetta threading (see STAR Methods). The longer Tpm1.6 and shorter Tpm3.2 models span the distance of about seven and six actin monomers, respectively (Figure 2).

To study the charge complementarity between actin and Tpms, we calculated their electrostatic surfaces together with that of actin. A positively charged region on actin resides in the proximity of the Tpm density (Figure S4). It corresponds to residues Lys326 and Lys328, which have been predicted to bind Tpms via salt bridges, alongside negatively charged Asp311[27,28] (see below). Most of the actin-facing side of both Tpm1.6 (Figure 2B) and Tpm3.2 (Figure 2C) is negatively charged. A notable exception is the N terminus, which is positively charged in both tropomyosin isoforms (Figure S1).

In the energy-minimized Rosetta models, the actin residues Lys326, Lys328, and Asp311 were observed to interact with both Tpms in most of the actin-binding sites (in total seven for Tpm1.6 and six for Tpm 3.2; Figure 2; Table 1). Lys326 and Lys328 interact with side chains of two glutamate residues (in one instance the side chain of an aspartate residue) in one of the two Tpm α-helices, separated approximately by one turn of the α-helix (four residues apart). The models also revealed another type of salt bridge, where Asp311 on actin interacts with a lysine residue on the Tpm.

Are there alternative binding modes between actin and Tpm to those described above? We tested this by sliding the Tpm coiled-coil models through the Tpm cryo-EM density at steps corresponding to one α-helical turn (~5.5 Å) and keeping the Tpm coil-coil interface fixed (see STAR Methods). We calculated the relative Rosetta binding energy for the actin-Tpm interface at each position (Figure S5). The models described above (no translation) had the lowest interface energies, supporting the notion that Tpm prefers these binding modes. After the Tpm chain had been translated by the distance of two actins (corresponding to 22 and 23 α-helical turns in Tpm1.6 and Tpm3.2, respectively), the same binding modes as described above were repeated. Sliding the Tpm sequences by the distance of one actin (corresponding to 12 α-helical turns in both Tpms), in turn, resulted in either the same (for Tpm1.6) or slightly higher (for Tpm3.2) energy. This alternate binding mode is feasible because the two α-helices in the coiled-coils alternate in making contacts to actin; in every second position, the other α-helix from the coiled-coil is proximal to actin. However, the phase of the α-helices differs between consecutive actin-binding sites (Figures 2B and 2C). While in some positions the salt bridges are maintained, in other positions none or fewer of the actin sidechain rotamers are able to accommodate the shift in the Tpm α-helix, disrupting the salt bridges. The changing phase of the α-helix is also consistent with the absence of backbone signal in the cryo-EM density maps.

To conclude, our modeling not only predicts the same actin residues (Lys326, Lys328, and Asp311) that have been indicated in Tpm binding earlier[27,28] but provides further insights into their role in binding. Lys326 and Lys328 exhibit at least two different rotamers, one pointing up and one down. These, together with

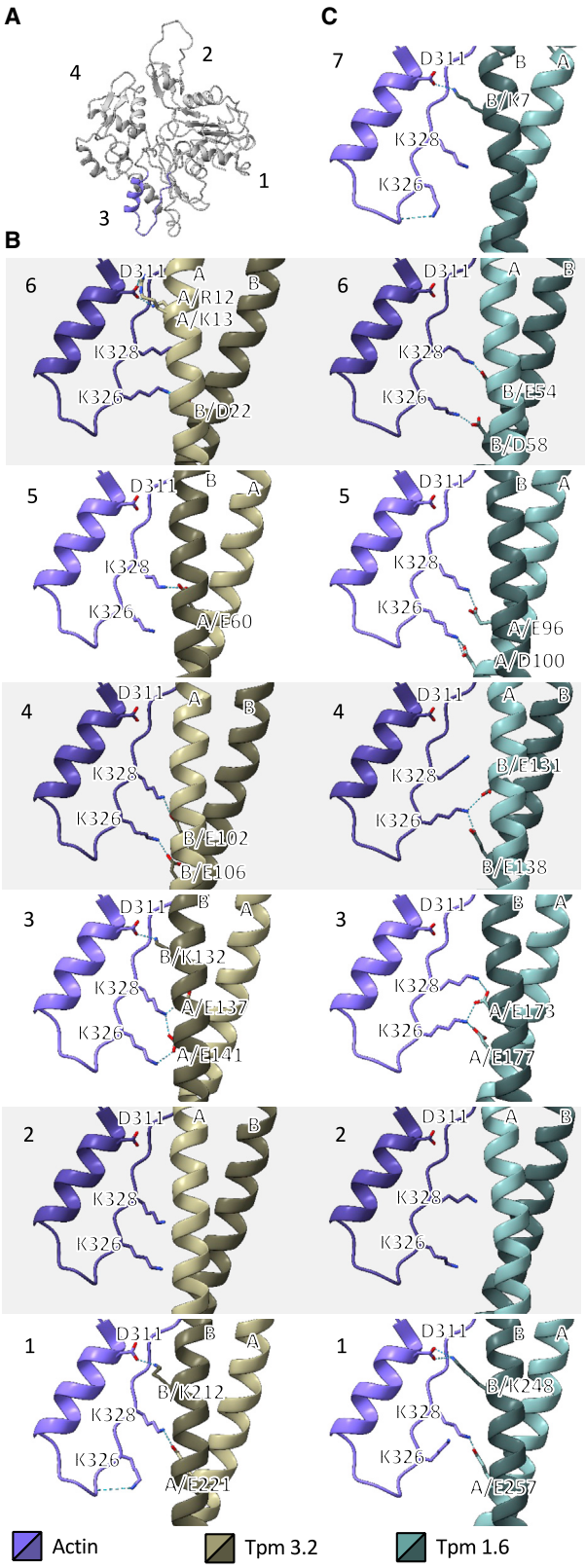

Figure 2. Models of the actin/non-muscle tropomyosin binding sites

(A) An atomic model of actin from actin:Tpm1.6 complex is shown as a ribbon. The different subdomains of actin are labeled 1–4. The helix-and-loop motif shown in a close-up in (B) and (C) in blue.

(B) Models of the binding sites between six actins and a single Tpm3.2 coiled-coil are shown. The two alpha-helices of the coiled-coil are labeled A and B. Sidechains are shown for actin residues D311, K326, and K328. Sidechains are also shown for those Tpm3.2 residues that are at hydrogen bonding distance. Hydrogen bonds predicted by the model are shown with dashed lines (cyan).

(C) The same rendering as in (B) is shown for seven actins and Tpm1.6. Please note that one of the interactions is absent in Tpm3.2 due to its shorter length. See also Figures S4 and S5.

the Tpm sequence at different actin interfaces, may provide enough flexibility to facilitate Tpm binding in different positions. Different Tpm sequences, vertical shift, and different sidechain rotamers likely accommodate the 5-Å lateral shift observed between the cryo-EM density between Tpm1.6 and Tpm3.2 tracks.

A structure-based rationale for the absence of isoform mixing between Tpm1.6 and Tpm3.2

Earlier studies provided evidence that Tpm1.6 and Tpm3.2 cannot co-polymerize on the same actin filament, and thus segregate to different actin filament structures in cells.[14,22] The molecular basis behind these observations, however, has remained unclear. We addressed this question by using the actin:Tpm1.6 and actin:Tpm3.2 models. Placement of two Tpm1.6 coiled-coil Rosetta minimum-energy models consecutively on the same side of the actin filament allows the juxtaposition of the N terminus from one dimer with the C terminus of the next dimer (Figure 3A). While the head-to-tail interaction is not revealed in our cryo-EM structures or Rosetta modeling, the juxtaposition shows that the phase of the Tpm1.6 α-helices and their positions match at the interaction site. The same is true for a homotypic juxtaposition of Tpm 3.2 coiled-coil with another Tpm 3.2 (Figure 3B). In contrast, a heterotypic juxtaposition of Tpm1.6 and Tpm3.2 consecutively on an actin filament shows that neither the phase of the α-helices, nor their position matches those of the α-helices in the next coiled-coil (Figures 3C and 3D). It is conceivable that both the phase of the α-helix and the position of the Tpm ends may play a role in promoting the formation of favorable head-to-tail interactions and further cooperative binding of the same isoform type on an actin filament. Thus, in addition to sequence-specific interactions between the N and C termini of Tpm dimers,[29–31] these geometrical factors indicated by our modeling are likely to play a crucial role in preventing heterotypic Tpm head-to-tail interactions. This hypothesis, based on the geometrical considerations and the observed 5-Å shift between Tpm1.6 and Tpm3.2 densities, requires further validation by cryo-EM of actin:Tpm1.6 and actin:Tpm3.2 complexes where the Tpm ends can be resolved. This could be possible by extending the approaches applied recently to visualize the muscle Tpm ends at low resolution in actin:Tpm:troponin complex.[9]

Comparison of structures reveals similarities and differences between non-muscle and muscle tropomyosin-binding modes

We next compared the structures of actin:Tpm1.6 and actin:Tpm3.2 to the previously reported complexes between actin

Table 1. Predicted salt bridges between actin and tropomyosin (Tpm) isoforms

	Actin	Tpm1.6		Tpm3.2	
Position	Residue	Residue	Chain	Residue	Chain
1	D311	K248	B	K212	B
1	K328	E257	A	E221	A
1	K326	–	–	–	–
2	D311	–	–	–	–
2	K328	–	–	–	–
2	K326	–	–	–	–
3	D311	–	–	K132	B
3	K328	E173	A	E137	A
3	K326	E177	A	E141	A
4	D311	–	–	–	–
4	K328	–	–	E102	B
4	K326	E131 + E138	B	E106	B
5	D311	–	–	–	–
5	K328	E96	A	E60	A
5	K326	D100	A	–	–
6	D311	–	–	R12 + K13	A
6	K328	E54	B	–	–
6	K326	D58	B	D22	B
7	D311	K7	B	N/A	N/A
7	K328	–	–	N/A	N/A
7	K326	–	–	N/A	N/A

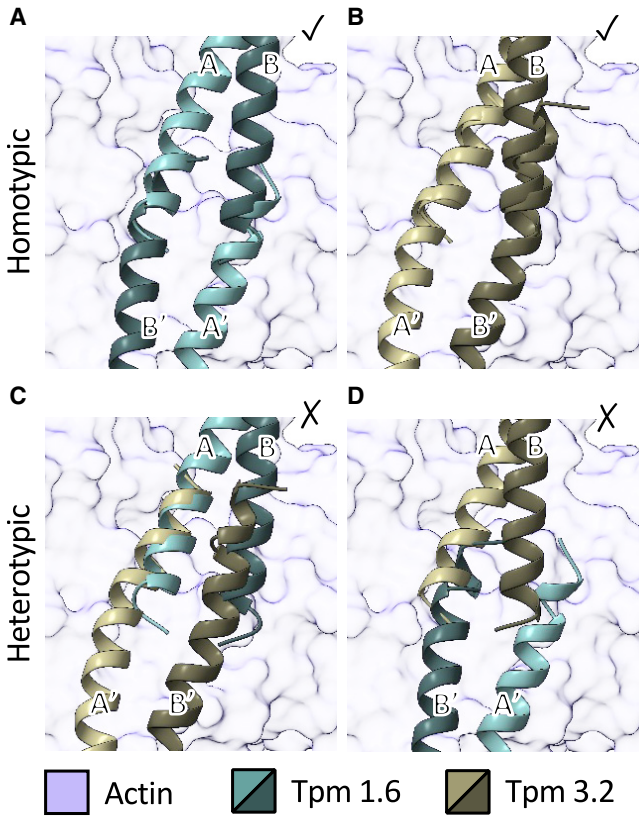

Figure 3. Visualizations of the tropomyosin ends

(A and B) Placement of two consecutive tropomyosins of the same kind (homotypic placement) are shown for Tpm1.6 (A) and for Tpm3.2 (B).

(C and D) Placement of two consecutive tropomyosins of the different kinds (heterotypic placement) are shown. In all panels the two α-helices of the tropomyosin coiled-coil are labeled with A and B. The helices in the adjacent coiled-coil are labeled with A′ and B′. In all cases a conformational change in the Tpm ends would be required to allow binding of the next coiled-coil in the filament to avoid overlap. However, in the heterotypic complexes, neither the phase of the α-helices nor their position matches those of the α-helices in the adjacent coiled-coil.

See also Figure S5.

and muscle Tpms. The long non-muscle isoform Tpm1.6 occupies nearly the same position on actin as the skeletal muscle Tpm1.1 (Figures 4A and 4B),[7] showing a shift of 2 Å in the direction of the filament long axis and rotation of 0.7° around the axis. This "A-state" position corresponds to the state of muscle Tpm on actin filament when no other proteins are present. In this context, it is important to note that muscle Tpm and non-muscle Tpm1.6 are encoded by the same *TPM1* gene, the only difference being that, as a result of alternative splicing, the last 27 amino acid residues of Tpm1.6 are different from those of Tpm1.1 (Figure S1). In conclusion, this comparison shows that the C-terminal part of Tpm1 is not required for binding to the A-state position, but rather that both Tpm1.1 and Tpm1.6 bind the same position presumably via equivalent interactions. The C-terminal part, which is quite different between Tpm1.1 and Tpm1.6, may however play a role in preventing the mixing of different isoforms and/or promoting the binding of the next tropomyosin dimer via head-to-tail interactions. Moreover, the non-conserved C-terminal region of skeletal muscle Tpm1.1 may contribute to interactions with the troponin complex, which is absent from non-muscle cells expressing Tpm1.6.

The position of non-muscle Tpm3.2, in turn, is between the A-state and the myosin-bound M-state observed in the muscle actin:Tpm complex[6,10] (Figures 4C and 4D). This state, denoted here as the A′-state, shows the Tpm3.2 shifted 7 Å along the filament long axis and rotated 8° around it (the rotation corresponding to a horizontal shift of ∼6 Å; see Figure 1E) relative to the muscle tropomyosin in the A-state (Figure 4C). For comparison, muscle Tpm in the M-state is shifted 23 Å and rotated 15° relative to the A-state (Figure 4D).

Interplay of non-muscle tropomyosins with ADF/cofilin

To evaluate if the different positions of Tpm1.6 (A-state) and Tpm3.2 (A′-state) on an actin filament affect their interactions with ADF/cofilin, we carried out further binding experiments.

ADF/cofilin binds actin filaments in a cooperative manner and severs filaments at the boundaries between free and ADF/cofilin-decorated segments.[32–34] ADF/cofilin and Tpms compete for actin binding, and Tpm isoforms protect actin filaments from ADF/cofilin-mediated severing to a different extent.[11,22,24] Interestingly, when the most abundant mammalian ADF/cofilin isoform, cofilin-1, is docked to Tpm-actin filaments by using earlier

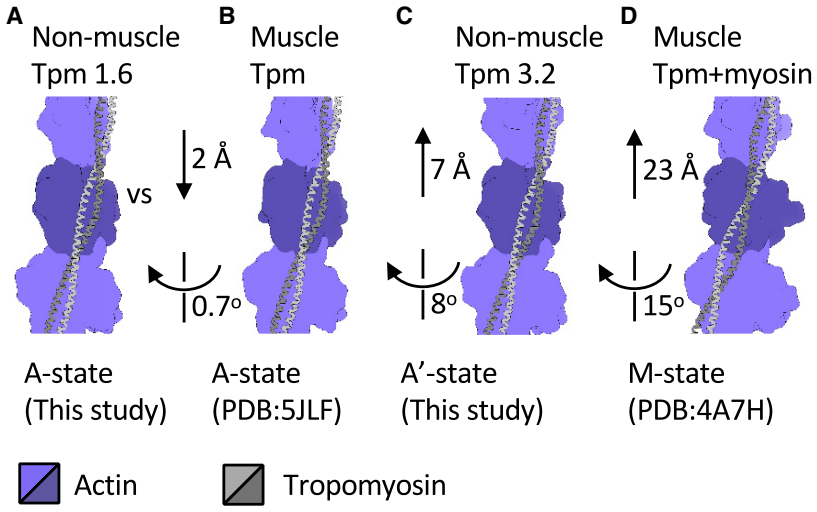

Figure 4. Comparison of the tropomyosin positions on the actin filament

(A–D) The position of Tpm1.6 in (A) (A-state) is compared with muscle tropomyosin in (B) (A-state), Tpm3.2 in (C) (A′-state), and to the one muscle tropomyosin from myosin-bound (not shown) structure in (D) (M-state). The shifts and rotations shown indicate the measured transformations taking the tropomyosin coiled-coils in (B)–(D) on the reference coiled-coil in (A).

structural information,[35] more pronounced steric clashes occur with Tpm1.6 than with Tpm3.2 (Figures 5A–5C). To directly test ADF/cofilin binding on actin filaments decorated either with Tpm1.6 or Tpm3.2, we first performed *in vitro* TIRF microscopy on sfGFP-fusions of Tpm1.6 and Tpm3.2, and mCherry-fusion of human cofilin-1. We prepared sfGFP-Tpm-decorated actin filaments, mixed these with mCherry-cofilin-1, and imaged the samples immediately after mixing by TIRF microscopy. At our experimental conditions, we observed both individual actin filaments and filament bundles (Figures S6C and S6D). Already at early time points, cofilin-1 segments were more visible on Tpm3.2-decorated actin filaments and filament bundles compared with Tpm1.6-decorated filaments and bundles, and these differences became more pronounced after 30-min incubation (Figures S6C and S6D). Because the *in vitro* TIRF microscopy experiments required fluorescently labeled Tpms, which may influence the effects of these proteins on cofilin-actin interactions, we next performed a pyrene-actin assay to monitor cofilin binding to actin filaments. Cofilin binding to pyrene-actin filaments results in the quenching of pyrene-actin fluorescence,[36] and when the assay is carried out in the absence of actin monomer-sequestering agents, or without diluting actin filaments below the critical concentration, the quenching of pyrene fluorescence predominantly reflects cofilin binding to actin filaments rather than filament depolymerization. We additionally carried out the assay at pH 6.6, where cofilin disassembles actin filaments less efficiently compared with neutral pH. Consistent with the TIRF experiments, this assay provided evidence that cofilin-1 binds to Tpm1.6-actin filaments with slower kinetics compared with Tpm3.2-actin filaments (Figure 5D). Finally, we carried out an actin filament co-sedimentation experiment, which demonstrated that at steady-state the amount of actin filament bound cofilin-1 is slightly lower in the presence of Tpm1.6 compared with Tpm3.2 (Figures 5E, S6A, and S6B). Together, these results provide evidence that Tpm1.6 and Tpm3.2 inhibit actin filament binding of ADF/cofilin to different extents, and that especially the kinetics of ADF/cofilin binding to actin filaments is much slower in the presence of Tpm1.6. These effects on ADF/cofilin binding may be at least partially due to the different actin filament binding interfaces of the two Tpm isoforms.

DISCUSSION

Different non-muscle Tpm isoforms have distinct cellular functions, and they provide specific functional features to the actin filaments.[3] However, the underlying structural principles have remained unknown. Moreover, the molecular basis by which different Tpm isoforms segregate to different actin filaments *in vitro*[22] has remained elusive. Cryo-EM and biochemical experiments on non-muscle β/γ-actin filaments decorated by two non-muscle Tpm isoforms allowed us to probe the mechanisms underlying their specific functions. Most importantly, we revealed that while Tpm1.6 and Tpm3.2 binding leaves the actin conformation unaltered, they follow different paths along the major groove of the actin filament. We speculate that this property of Tpms contributes to their different biochemical functions and specific role in cells.

The different positioning of Tpm1.6 and Tpm3.2 along the actin filament provides a plausible explanation for why these two Tpm isoforms cannot co-polymerize with each other on actin filaments. This is because the heterotypic juxtaposition of Tpm1.6 and Tpm3.2 on an actin filament shows that neither the phase of the α-helices nor their positions match with those of the α-helices in the adjacent tropomyosin coiled-coil. Therefore, whereas the N and C termini of Tpm dimers of the same isoform can generate proper head-to-tail oligomers, the N and C termini of Tpm1.6 and Tpm3.2 isoforms are out of the registry for head-to-tail interactions. In addition to these geometrical factors, also sequence-specific interactions between Tpm N and C termini contribute to their co-polymerization on actin filaments. However, because the C-terminal regions of Tpm1.6 and Tpm3.2 are nearly identical to each other, and for example much more similar than the ones between Tpm1.1 and Tpm1.6 (Figure S1), we speculate that in the case of Tpm1.6 and Tpm3.2, the lack of isoform mixing must result mainly from their different positioning along the actin filament. In the future, it will be interesting to examine if also other most abundant non-muscle Tpm isoforms are "out of register" with each other on an actin filament, as well as to study the specific roles of N- and C-terminal sequences of Tpms in their co-polymerization.

Earlier biochemical studies provided evidence that Tpm1.6 displays a much more stable association with actin filaments *in vitro* compared with Tpm3.2.[22] This may be partially due to the presence of seven actin-binding sites in Tpm1.6 vs. six

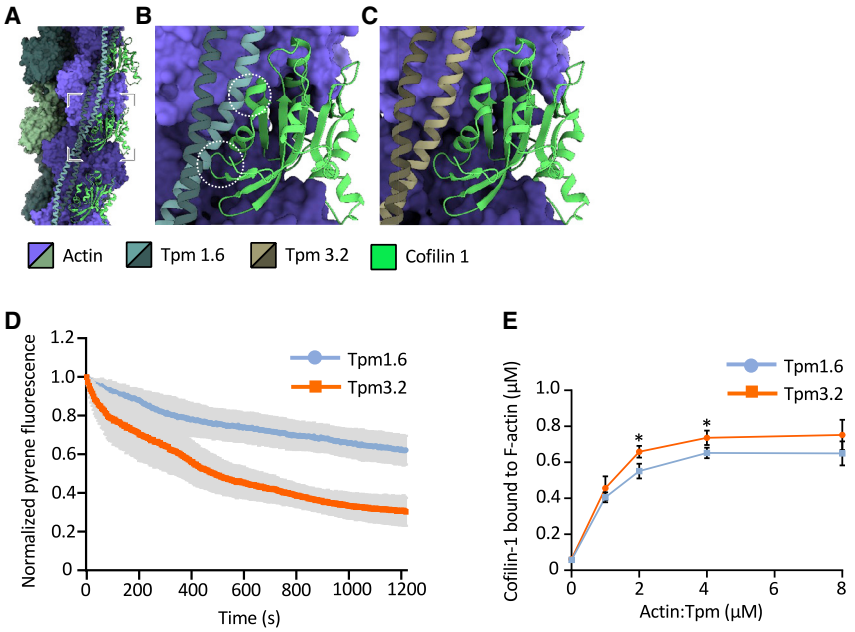

Figure 5. Influence of Tpm1.6. and Tpm3.2 on cofilin binding to actin filaments

(A) A model of actin/Tpm1.6 complex with three copies of cofilin-1 (PDB: 5YU8).

(B) A close-up of the area indicated in (A). Tpm1.6 binding site overlaps (dashed circles) with the one of cofilin-1.

(C) The same view as in (B) is shown for actin/Tpm3.2 complex together with cofilin-1. No major clashes are evident.

(D) Time courses of pyrene-actin quenching by cofilin-1 in the presence of actin:Tpm1.6 and actin:Tpm3.2 filaments. The assay was carried out in the absence of actin monomer-sequestering agents at pH 6.6, so the quenching of pyrene-fluorescence is expected to reflect the kinetics of cofilin binding to actin filaments rather than filament disassembly. Both curves show the mean of seven independent repeats, and error bars represent the standard deviation. The final concentrations of actin (95% β/γ-actin and 5% skeletal muscle pyrene-actin) and cofilin-1 were 2 μM.

(E) Co-sedimentation assay showing cofilin-1 binding to actin filaments decorated by Tpm1.6 and Tpm3.2. Cofilin-1 concentration was 1 μM, and the concentration of actin (mixed with Tpm1.6 or Tpm3.2 at 4.7:1 and 4:1 ratios, respectively) was varied between 0 and 8 μM. The data are averaged values from three independent co-sedimentation experiments, and the error bars represent standard deviations. *p values = 0.0234 (2 μM actin:Tpm1.6 vs. 2 μM actin:Tpm3.2) and 0.0427 (4 μM actin:Tpm1.6 vs. 4 μM actin:Tpm3.2). The significance was determined using two-tailed unpaired t test with 95% confidence intervals.

See also Figure S6.

such sites in Tpm3.2. Additionally, Tpm1.6 occupies the "A-state" position on an actin filament, whereas Tpm3.2 is shifted toward the M-state position, which at least in the case of muscle Tpm is energetically unfavorable. Because the central regions of Tpm1.6 and Tpm3.2 are highly conserved between each other and with muscle Tpm1.1 (Figure S1), it is likely that the variable regions adjacent to N and C termini are responsible for the different positioning of Tpm1.6 and Tpm3.2 on the actin filament. Moreover, possible differences in the head-to-tail interactions may be responsible for the slow off-rate of Tpm1.6 from actin filaments compared with the relatively dynamic association of Tpm3.2 with actin filaments.

Our study sheds light on the different effects of Tpm1.6 and Tpm3.2 isoforms on ADF/cofilin and myosin II. We propose that, due to the larger overlap between Tpm1.6 and ADF/cofilin on actin filament, compared with Tpm3.2 and ADF/cofilin, Tpm1.6 prevents more efficiently ADF/cofilin binding to actin filament (Figures 5 and S6). This could explain why Tpm1.6 protects actin filaments more efficiently from ADF/cofilin-mediated disassembly compared with Tpm3.2.[22] Interestingly, Tpm3.2 activates myosin II while Tpm1.6 does not,[22] and there seems to be a larger overlap between myosin and Tpm1.6 than between myosin and Tpm3.2 on an actin filament. Thus, it is possible that Tpm3.2 increases the affinity or cooperativity of myosin II binding to actin filaments, and this may be related to the different positioning of Tpm3.2 and Tpm1.6 on actin filaments. Alternatively, the different effects of Tpm1.6 and Tpm3.2 on actin-induced myosin II ATPase activity may result from sequence-specific interactions between Tpm3.2 and myosin II motor domain that could enhance ATPase activation of the myosin. However, future studies are needed to uncover the precise mechanism by which certain non-muscle Tpms, including Tpm3.2, increase the actin-dependent myosin II steady-state ATPase rate.

In conclusion, our work suggests that both the positioning of the Tpm isoform on actin filament, as well as sequence-specific interactions between Tpms and other actin-binding proteins, contribute to specific functions of different Tpm isoforms. In this context, it is important to note that non-muscle Tpms have so far been studied only in the context of a handful of actin-binding proteins, but they are likely to also control the activities of a large array of other actin-binding proteins, including the many members of the myosin family. Thus, more work is required to understand how non-muscle Tpms regulate the interactions with various cytoskeletal proteins with actin filaments. Moreover, it will be important to determine the structures of other non-muscle actin-Tpm filaments and uncover the molecular basis of their distinct biological and biochemical activities. Finally, it will be interesting to determine the high-resolution structures of native non-muscle Tpms to uncover the precise mechanisms by which properly post-translationally modified Tpms form head-to-tail interactions on actin filaments.

Limitations of the study

The symmetry mismatches in the actin:Tpm assemblies, due to the binding of one Tpm molecule to six or seven actin monomers, hampered resolving the side chains of amino acid residues of Tpms in our structures, in addition to the ends of the Tpm coiled-coils. Moreover, this work, as well as earlier biochemical studies, were performed using Tpms produced in *E. coli.* These Tpms contain an acetylation-mimic Met-Ala-Ser sequence in the N terminus. Tpms purified from mammalian cells that harbor

native post-translational modifications, however, display slightly different affinities on actin filaments.[37] Thus, also the dynamics of native Tpms on actin filaments may exhibit small differences from the ones produced in *E. coli*.

STAR★METHODS

Detailed methods are provided in the online version of this paper and include the following:

- KEY RESOURCES TABLE
- RESOURCE AVAILABILITY
  - Lead contact
  - Materials availability
  - Data and code availability
- EXPERIMENTAL MODEL AND SUBJECT DETAILS
  - Bacterial strains
- METHOD DETAILS
  - Protein purification
  - Co-sedimentation assays
  - Pyrene-actin quenching assay
  - *In-vitro* TIRF microscopy
  - Cryo-EM sample preparation, data collection and image processing
  - Atomic model building and molecular modeling
- QUANTIFICATION AND STATISTICAL ANALYSIS

SUPPLEMENTAL INFORMATION

Supplemental information can be found online at https://doi.org/10.1016/j.celrep.2022.111900.

ACKNOWLEDGMENTS

We thank Pasi Laurinmäki and Benita Löflund for technical assistance in cryo-EM. The facilities and expertise of the HiLIFE cryo-EM unit at the University of Helsinki, a member of Instruct-ERIC Center Finland, FINStruct, and Biocenter Finland are gratefully acknowledged. The authors wish to acknowledge CSC – IT Center for Science, Finland, for computational resources. This study was supported by grants from Academy of Finland (Center of Excellence grant 346133 to P.L.) and Sigrid Jusélius Foundation (4708344 to P.L.). Work in the laboratory of J.T.H. was supported by Helsinki Institute of Life Science HiLIFE. The graphical abstract was created with BioRender.

AUTHOR CONTRIBUTIONS

Conceptualization, F.D., P.L., and J.T.H. Formal analysis, M.S., S.B.K., T.K., and J.T.H. Investigation, M.S., S.B.K., R.G., K.K., T.K., and K.E. Writing – original draft, S.B.K., P.L., and J.T.H. Writing – review & editing, M.S., S.B.K., P.L., and J.T.H. Visualization, J.T.H. Funding acquisition, P.L. Resources, S.B.K., E.K., and K.K. Supervision, F.D., P.L., and J.T.H.

DECLARATION OF INTERESTS

The authors declare no competing interests.

INCLUSION AND DIVERSITY

We support inclusive, diverse, and equitable conduct of research.

Received: May 12, 2022
Revised: November 3, 2022
Accepted: December 7, 2022

REFERENCES

1. Blanchoin, L., Boujemaa-Paterski, R., Sykes, C., and Plastino, J. (2014). Actin dynamics, architecture, and mechanics in cell motility. Physiol. Rev. *94*, 235–263.
2. Boiero Sanders, M., Antkowiak, A., and Michelot, A. (2020). Diversity from similarity: cellular strategies for assigning particular identities to actin filaments and networks. Open Biol. *10*, 200157.
3. Gunning, P.W., Ghoshdastider, U., Whitaker, S., Popp, D., and Robinson, R.C. (2015). The evolution of compositionally and functionally distinct actin filaments. J. Cell Sci. *128*, 2009–2019.
4. Gunning, P.W., Hardeman, E.C., Lappalainen, P., and Mulvihill, D.P. (2015). Tropomyosin–master regulator of actin filament function in the cytoskeleton. J. Cell Sci. *128*, 2965–2974.
5. Geeves, M.A. (2012). 4.13 thin filament regulation. Comprehensive Biophys. *4*, 251–267.
6. Behrmann, E., Müller, M., Penczek, P.A., Mannherz, H.G., Manstein, D.J., and Raunser, S. (2012). Structure of the rigor actin-tropomyosin-myosin complex. Cell *150*, 327–338.
7. Von der Ecken, J., Müller, M., Lehman, W., Manstein, D.J., Penczek, P.A., and Raunser, S. (2015). Structure of the F-actin–tropomyosin complex. Nature *519*, 114–117.
8. Doran, M.H., Pavadai, E., Rynkiewicz, M.J., Walklate, J., Bullitt, E., Moore, J.R., Regnier, M., Geeves, M.A., and Lehman, W. (2020). Cryo-EM and molecular docking shows myosin loop 4 contacts actin and tropomyosin on thin filaments. Biophys. J. *119*, 821–830.
9. Yamada, Y., Namba, K., and Fujii, T. (2020). Cardiac muscle thin filament structures reveal calcium regulatory mechanism. Nat. Commun. *11*, 153–159.
10. Risi, C., Schäfer, L.U., Belknap, B., Pepper, I., White, H.D., Schröder, G.F., and Galkin, V.E. (2021). High-resolution cryo-EM structure of the cardiac actomyosin complex. Structure *29*, 50–60.e4.
11. Ono, S., and Ono, K. (2002). Tropomyosin inhibits ADF/cofilin-dependent actin filament dynamics. J. Cell Biol. *156*, 1065–1076.
12. Coulton, A.T., East, D.A., Galinska-Rakoczy, A., Lehman, W., and Mulvihill, D.P. (2010). The recruitment of acetylated and unacetylated tropomyosin to distinct actin polymers permits the discrete regulation of specific myosins in fission yeast. J. Cell Sci. *123*, 3235–3243.
13. Christensen, J.R., Hocky, G.M., Homa, K.E., Morganthaler, A.N., Hitchcock-DeGregori, S.E., Voth, G.A., and Kovar, D.R. (2017). Competition between Tropomyosin, Fimbrin, and ADF/Cofilin drives their sorting to distinct actin filament networks. Elife *6*, e23152.
14. Tojkander, S., Gateva, G., Schevzov, G., Hotulainen, P., Naumanen, P., Martin, C., Gunning, P.W., and Lappalainen, P. (2011). A molecular pathway for myosin II recruitment to stress fibers. Curr. Biol. *21*, 539–550.
15. Kumari, R., Jiu, Y., Carman, P.J., Tojkander, S., Kogan, K., Varjosalo, M., Gunning, P.W., Dominguez, R., and Lappalainen, P. (2020). Tropomodulins control the balance between Protrusive and Contractile structures by stabilizing actin-tropomyosin filaments. Curr. Biol. *30*, 767–778.e5.
16. Meiring, J.C.M., Bryce, N.S., Niño, J.L.G., Gabriel, A., Tay, S.S., Hardeman, E.C., Biro, M., and Gunning, P.W. (2019). Tropomyosin concentration but not formin nucleators mDia1 and mDia3 determines the level of tropomyosin incorporation into actin filaments. Sci. Rep. *9*, 6504–6511.
17. Bryce, N.S., Schevzov, G., Ferguson, V., Percival, J.M., Lin, J.J.-C., Matsumura, F., Bamburg, J.R., Jeffrey, P.L., Hardeman, E.C., Gunning, P., and Weinberger, R.P. (2003). Specification of actin filament function and molecular composition by tropomyosin isoforms. Mol. Biol. Cell *14*, 1002–1016.
18. Bach, C.T.T., Creed, S., Zhong, J., Mahmassani, M., Schevzov, G., Stehn, J., Cowell, L.N., Naumanen, P., Lappalainen, P., Gunning, P.W., and O'Neill, G.M. (2009). Tropomyosin isoform expression regulates the transition of adhesions to determine cell speed and direction. Mol. Cell Biol. *29*, 1506–1514.

19. Gallant, C., Appel, S., Graceffa, P., Leavis, P., Lin, J.J.-C., Gunning, P.W., Schevzov, G., Chaponnier, C., DeGnore, J., Lehman, W., and Morgan, K.G. (2011). Tropomyosin variants describe distinct functional subcellular domains in differentiated vascular smooth muscle cells. Am. J. Physiol. Cell Physiol. *300*, C1356–C1365.

20. Johnson, M., East, D.A., and Mulvihill, D.P. (2014). Formins determine the functional properties of actin filaments in yeast. Curr. Biol. *24*, 1525–1530.

21. Cagigas, M.L., Bryce, N.S., Ariotti, N., Brayford, S., Gunning, P.W., and Hardeman, E.C. (2022). Correlative cryo-ET identifies actin/tropomyosin filaments that mediate cell-substrate adhesion in cancer cells and mechanosensitivity of cell proliferation. Nat. Mater. *21*, 120–128.

22. Gateva, G., Kremneva, E., Reindl, T., Kotila, T., Kogan, K., Gressin, L., Gunning, P.W., Manstein, D.J., Michelot, A., and Lappalainen, P. (2017). Tropomyosin isoforms specify functionally distinct actin filament populations in vitro. Curr. Biol. *27*, 705–713.

23. Pathan-Chhatbar, S., Taft, M.H., Reindl, T., Hundt, N., Latham, S.L., and Manstein, D.J. (2018). Three mammalian tropomyosin isoforms have different regulatory effects on nonmuscle myosin-2B and filamentous β-actin in vitro. J. Biol. Chem. *293*, 863–875.

24. Jansen, S., and Goode, B.L. (2019). Tropomyosin isoforms differentially tune actin filament length and disassembly. Mol. Biol. Cell *30*, 671–679.

25. He, S., and Scheres, S.H.W. (2017). Helical reconstruction in RELION. J. Struct. Biol. *198*, 163–176. https://doi.org/10.1016/j.jsb.2017.02.003.

26. Chou, S.Z., and Pollard, T.D. (2019). Mechanism of actin polymerization revealed by cryo-EM structures of actin filaments with three different bound nucleotides. Proc. Natl. Acad. Sci. USA *116*, 4265–4274.

27. Lehman, W., Moore, J.R., Campbell, S.G., and Rynkiewicz, M.J. (2019). The effect of tropomyosin mutations on actin-tropomyosin binding: in search of lost time. Biophys. J. *116*, 2275–2284.

28. Pavadai, E., Lehman, W., and Rynkiewicz, M.J. (2020). Protein-protein docking reveals dynamic interactions of tropomyosin on actin filaments. Biophys. J. *119*, 75–86.

29. Greenfield, N.J., Huang, Y.J., Swapna, G.V.T., Bhattacharya, A., Rapp, B., Singh, A., Montelione, G.T., and Hitchcock-DeGregori, S.E. (2006). Solution NMR structure of the junction between tropomyosin molecules: implications for actin binding and regulation. J. Mol. Biol. *364*, 80–96.

30. Rao, J.N., Rivera-Santiago, R., Li, X.E., Lehman, W., and Dominguez, R. (2012). Structural analysis of smooth muscle tropomyosin α and β isoforms. J. Biol. Chem. *287*, 3165–3174.

31. Li, X.E., Orzechowski, M., Lehman, W., and Fischer, S. (2014). Structure and flexibility of the tropomyosin overlap junction. Biochem. Biophys. Res. Commun. *446*, 304–308.

32. Andrianantoandro, E., and Pollard, T.D. (2006). Mechanism of actin filament turnover by severing and nucleation at different concentrations of ADF/cofilin. Mol. Cell *24*, 13–23.

33. Suarez, C., Roland, J., Boujemaa-Paterski, R., Kang, H., McCullough, B.R., Reymann, A.-C., Guérin, C., Martiel, J.-L., De la Cruz, E.M., and Blanchoin, L. (2011). Cofilin tunes the nucleotide state of actin filaments and severs at bare and decorated segment boundaries. Curr. Biol. *21*, 862–868.

34. Wioland, H., Guichard, B., Senju, Y., Myram, S., Lappalainen, P., Jégou, A., and Romet-Lemonne, G. (2017). ADF/cofilin accelerates actin dynamics by severing filaments and promoting their depolymerization at both ends. Curr. Biol. *27*, 1956–1967.e7.

35. Tanaka, K., Takeda, S., Mitsuoka, K., Oda, T., Kimura-Sakiyama, C., Maéda, Y., and Narita, A. (2018). Structural basis for cofilin binding and actin filament disassembly. Nat. Commun. *9*, 1860–1912.

36. Carlier, M.-F., Laurent, V., Santolini, J., Melki, R., Didry, D., Xia, G.-X., Hong, Y., Chua, N.-H., and Pantaloni, D. (1997). Actin depolymerizing factor (ADF/cofilin) enhances the rate of filament turnover: implication in actin-based motility. J. Cell Biol. *136*, 1307–1322.

37. Carman, P.J., Barrie, K.R., and Dominguez, R. (2021). Novel human cell expression method reveals the role and prevalence of posttranslational modification in nonmuscle tropomyosins. J. Biol. Chem. *297*, 101154.

38. Kokate, S.B., Ciuba, K., Tran, V.D., Kumari, R., Tojkander, S., Engel, U., Kogan, K., Kumar, S., and Lappalainen, P. (2022). Caldesmon controls stress fiber force-balance through dynamic cross-linking of myosin II and actin-tropomyosin filaments. Nat. Commun. *13*, 6032–6120.

39. Zheng, S.Q., Palovcak, E., Armache, J.-P., Verba, K.A., Cheng, Y., and Agard, D.A. (2017). MotionCor2: anisotropic correction of beam-induced motion for improved cryo-electron microscopy. Nat. Methods *14*, 331–332.

40. Rohou, A., and Grigorieff, N. (2015). CTFFIND4: Fast and accurate defocus estimation from electron micrographs. J. Struct. Biol. *192*, 216–221.

41. Waterhouse, A., Bertoni, M., Bienert, S., Studer, G., Tauriello, G., Gumienny, R., Heer, F.T., de Beer, T.A.P., Rempfer, C., Bordoli, L., et al. (2018). SWISS-MODEL: homology modelling of protein structures and complexes. Nucleic Acids Res. *46*, W296–W303. https://doi.org/10.1093/nar/gky427.

42. Casañal, A., Lohkamp, B., and Emsley, P. (2020). Current developments in Coot for macromolecular model building of electron cryo-microscopy and crystallographic data. Protein Sci. *29*, 1055–1064.

43. Croll, T.I. (2018). ISOLDE: a physically realistic environment for model building into low-resolution electron-density maps. Acta Crystallogr. D Struct. Biol. *74*, 519–530. https://doi.org/10.1107/S2059798318002425.

44. Afonine, P.V., Poon, B.K., Read, R.J., Sobolev, O.V., Terwilliger, T.C., Urzhumtsev, A., and Adams, P.D. (2018). Real-space refinement in PHENIX for cryo-EM and crystallography. Acta Crystallogr. D Struct. Biol. *74*, 531–544. https://doi.org/10.1107/S2059798318006551.

45. Pettersen, E.F., Goddard, T.D., Huang, C.C., Meng, E.C., Couch, G.S., Croll, T.I., Morris, J.H., and Ferrin, T.E. (2021). UCSF ChimeraX: structure visualization for researchers, educators, and developers. Protein Sci. *30*, 70–82.

46. Wang, R.Y.-R., Song, Y., Barad, B.A., Cheng, Y., Fraser, J.S., and DiMaio, F. (2016). Automated structure refinement of macromolecular assemblies from cryo-EM maps using Rosetta. Elife *5*, e17219.

47. Janco, M., Bonello, T.T., Byun, A., Coster, A.C.F., Lebhar, H., Dedova, I., Gunning, P.W., and Böcking, T. (2016). The impact of tropomyosins on actin filament assembly is isoform specific. BioArchitecture *6*, 61–75.

48. Zivanov, J., Nakane, T., Forsberg, B.O., Kimanius, D., Hagen, W.J., Lindahl, E., and Scheres, S.H. (2018). New tools for automated high-resolution cryo-EM structure determination in RELION-3. Elife *7*, e42166.

49. Williams, C.J., Headd, J.J., Moriarty, N.W., Prisant, M.G., Videau, L.L., Deis, L.N., Verma, V., Keedy, D.A., Hintze, B.J., Chen, V.B., et al. (2018). MolProbity: more and better reference data for improved all-atom structure validation. Protein Sci. *27*, 293–315. https://doi.org/10.1002/pro.3330.

50. Jumper, J., Evans, R., Pritzel, A., Green, T., Figurnov, M., Ronneberger, O., Tunyasuvunakool, K., Bates, R., Žídek, A., Potapenko, A., et al. (2021). Highly accurate protein structure prediction with AlphaFold. Nature *596*, 583–589. https://doi.org/10.1038/s41586-021-03819-2.

51. Song, Y., DiMaio, F., Wang, R.Y.-R., Kim, D., Miles, C., Brunette, T., Thompson, J., and Baker, D. (2013). High-resolution comparative modeling with RosettaCM. Structure *21*, 1735–1742.

52. Conway, P., Tyka, M.D., DiMaio, F., Konerding, D.E., and Baker, D. (2014). Relaxation of backbone bond geometry improves protein energy landscape modeling. Protein Sci. *23*, 47–55.

STAR★METHODS

KEY RESOURCES TABLE

REAGENT or RESOURCE	SOURCE	IDENTIFIER
Bacterial and virus strains		
E.coli XL10-Gold ultracompetent cells	Agilent	Cat#200315
E.coli BL21(DE3) chemically competent cells	Novagen	Cat#69450
Chemicals, peptides, and recombinant proteins		
Non-muscle β/γ-actin (Human platelets)	Cytoskeleton Inc.	Cat#APHL99
Pyrene-actin (Rabbit skeletal muscle)	Cytoskeleton Inc.	Cat#AP05-B
Tagged and non-tagged Tpm and cofilin-1 proteins	Gateva et al.,[22] 2017; Kokate et al.,[38] 2022	Tagged: mCherry-Tpm1.6- pPL1150 mCherry-Tpm3.2- pPL1154 GFP-cofilin-1- pPL1643 Non-tagged: Tpm1.6- pPL1138 Tpm3.2- pPL1141 Cofilin-1- pPL0092
Protease inhibitor cocktail	Sigma-Aldrich	Cat#P2714
Critical commercial assays		
4%–20% gradient SDS-PAGE gels	Bio-Rad	Cat#4561096
QC Colloidal Coomassie stain	Bio-Rad	Cat#1610803
Deposited data		
Non-muscle F-actin decorated with non-muscle tropomyosin 1.6, cryo-EM map	This study	EMDB: EMD-14957
Non-muscle F-actin decorated with non-muscle tropomyosin 1.6, atomic model	This study	PDB: 7ZTC
Non-muscle F-actin decorated with non-muscle tropomyosin 3.2, cryo-EM map	This study	EMDB: EMD-14958
Non-muscle F-actin decorated with non-muscle tropomyosin 3.2, atomic model	This study	PDB: 7ZTD
Recombinant DNA		
Tagged and non-tagged Tpm and cofilin-1 DNA constructs	Gateva et al.,[22] 2017; Kokate et al.,[38] 2022	Tagged: mCherry-Tpm1.6- pPL1150 mCherry-Tpm3.2- pPL1154 GFP-cofilin-1- pPL1643 Non-tagged: Tpm1.6- pPL1138 Tpm3.2- pPL1141 Cofilin-1- pPL0092
Software and algorithms		
Fiji ImageJ	N/A	https://imagej.net/software/fiji/
Microsoft Excel	Microsoft	N/A
GraphPad Prism	GraphPad Software	https://www.graphpad.com/scientific-software/prism/
RELION	He & Scheres,[25] 2017	https://www2.mrc-lmb.cam.ac.uk/relion/
MotionCor2	Zheng et al.,[39] 2017	http://msg.ucsf.edu/software
CTFFIND4	Rohou and Grigorieff,[40] 2015	http://grigoriefflab.janelia.org/ctffind4
SWISS-MODEL	Waterhouse et al.,[41] 2018	https://swissmodel.expasy.org
Coot	Casañal et al.,[42] 2020	https://www2.mrc-lmb.cam.ac.uk/personal/pemsley/coot/
ISOLDE	Croll,[43] 2018	https://isolde.cimr.cam.ac.uk/
Phenix	Afonine et al.,[44] 2018	https://phenix-online.org/documentation/reference/real_space_refine.html
UCSF ChimeraX	Pettersen et al.,[45] 2021	https://www.cgl.ucsf.edu/chimerax/
ROSETTA	Wang et al.,[46] 2016	https://www.rosettacommons.org

RESOURCE AVAILABILITY

Lead contact

Further information and requests for resources and reagents should be directed to and will be fulfilled by the lead contact, Pekka Lappalainen (pekka.lappalainen@helsinki.fi).

Materials availability

This study did not generate new unique reagents.

Data and code availability

Cryo-EM maps and atomic models have been deposited at Electron Microscopy DataBank (EMDB) and Protein DataBank (PDB) and are publicly available as of the date of publication. Accession codes are listed in the key resources table. Any additional information required to reanalyze the data reported in this paper is available from the lead contact upon request. This paper does not report original code.

EXPERIMENTAL MODEL AND SUBJECT DETAILS

Bacterial strains

The bacterial expression plasmids available from previous studies (plasmid details are mentioned in the STAR Methods-key resources table) were transformed into *E.coli* BL21-DE3 chemically competent cells (#69450, Novagen) for protein expression followed by purification.

METHOD DETAILS

Protein purification

The plasmids for the structural and biochemical studies of tagged and non-tagged human tropomyosins Tpm1.6 and Tpm3.2 were available from the previous work.[22,38] Non-tagged Tpms were purified as per a published method.[47] Briefly, non-tagged Tpm constructs were expressed in *E.coli* BL21-DE3 bacterial expression system in 1 L Luria Bertani broth (2X) containing ampicillin (100 μg/mL) and was grown until the $O.D_{600}$ reached 0.7–0.8. The grown culture was further induced with 1 mM IPTG final concentration at 37°C for 3 h. Cells expressing untagged Tpms were harvested by centrifugation (4000× g, 4°C, 15 min, JS 4.2 rotor, J6-MI centrifuge, Beckman Coulter) and resuspended in lysis buffer (20 mM Na_2PO_4, 500 mM NaCl, 5 mM $MgCl_2$, 1 mM DTT and 1× protease inhibitor cocktail). The cells were lysed thoroughly by sonicating on ice (4 × 30s) until the bacterial suspension turned comparatively transparent. The cell lysate was heated in a water bath set at 80°C for 8 min. The heat-treated lysate was cooled to room temperature in a water bath. The supernatant containing Tpms was cleared from denatured proteins and cell debris by centrifugation at 47,810× g, 4°C for 45 min (F21S-8x50 rotor, Sorvall LYNX 4000, Thermo Fisher Scientific). Tpms were acid precipitated from the supernatant at pH 4.7 using 2 M HCl. The precipitated materials containing Tpms was centrifuged at 3900× g, 4°C for 12 min (F21S-8x50 rotor, Sorvall LYNX 4000, Thermo Fisher Scientific). The pellet was resuspended in a resuspension buffer (100 mM Tris-Cl pH 7.5, 500 mM NaCl, 5 mM $MgCl_2$, 1 mM DTT, 1 mM NaN_3). To dissolve the pellet completely, the buffer was readjusted to pH 7.0 using 1 M NaOH. The acid precipitation was repeated two more times to remove impurities and to obtain a white pellet. The pellet was resuspended in the resuspension buffer and filtered using a 0.22-μm membrane filter. Dialysis was performed overnight in a dialysis buffer (20 mM Tris-HCl pH 7.5, 500 mM NaCl, 0.5 mM DTT) using a 10-kDa molecular cutoff membrane (#88243, SnakeSkin™ Dialysis Tubing, 10MWCO, Thermo Fisher Scientific). The next day, a 4-mL SP QFF anion exchange column was equilibrated with 4 column volumes of anion exchange wash buffer (20 mM Tris-HCl pH 7.5, 10 mM NaCl, 0.5 mM DTT) and the supernatant was loaded onto the column at 2 mL/min loading speed. The column was washed with 4 column volumes of wash buffer. The column was further equilibrated with anion exchange elution buffer (20 mM Tris, pH 7.5, 1 M NaCl, 0.5 mM DTT) and Tpm was collected in the flow through. Samples from peak fractions were collected and analyzed by SDS-PAGE based on which the fractions were pooled together. The pooled fraction was diluted 4 times with hydroxyapatite wash buffer (10 mM Na_2PO_4 pH 7.0, 1 M NaCl, 0.5 mM DTT) and loaded onto an equilibrated hydroxyapatite column with 0.5 mL/min loading speed. The column was washed with 4 column volumes of hydroxyapatite wash buffer and the protein was eluted in a 10 mM–240 mM phosphate gradient against hydroxyapatite elution buffer (240 mM Na_2PO_4 pH 7.0, 1 M NaCl, 0.5 mM DTT). The eluted fractions were analyzed by SDS-PAGE and the fractions containing Tpm protein were pooled together. The acidification procedure was repeated twice to obtain pure protein. The precipitate was pelleted at 3900× g, 4°C for 12 min. The pellet was resuspended in dialysis buffer (20 mM Tris-HCl pH 7.0, 100 mM KCl, 5 mM $MgCl_2$, 0.5 mM DTT, 0.02% NaN_3) and dialyzed overnight at 4°C. The supernatant containing pure protein was concentrated using 30 MWCO column concentrator (Amicon Ultra-15, Merck Millipore). Purified protein concentration was measured using spectrophotometer (NanoDrop ND-1000 spectrophotometer, Thermo Fisher Scientific), fluorimetry and densitometry methods. The protein aliquots were flash frozen in liquid nitrogen and stored at −80°C.

The His-tagged sfGFP and mCherry fused tropomyosin and Cofilin-1 constructs were expressed in *E.coli* BL-21 (DE3) cells in 1 L auto-induction media at 37°C till $O.D_{600}$ reached 0.7–0.8 after which the cells were induced at 28°C for 24 h. The cells were harvested

by centrifugation at 4000× g, 4°C, 15 min (JS 4.2 rotor, J6-MI centrifuge, Beckman Coulter) and resuspended in Ni-NTA binding buffer (50 mM Tris-HCl pH 7.5, 300 mM NaCl, 10 mM imidazole, 1 mM DTT) and 1× protease inhibitor cocktail. Cells were lysed by sonication and cell debris was pelleted at 4000× g, 4°C for 15 min (JS 4.2 rotor, J6-MI centrifuge, Beckman Coulter). The his-tagged Tpm1.6 and Tpm3.2 were purified with Ni-NTA agarose beads (Qiagen) as per the manufacturer's protocol. Ni-NTA agarose beads were first washed 2 times with Ni-binding buffer and centrifuged at 3000× g, 4°C for 5 min and the beads were suspended in an equal volume of binding buffer. The Ni-NTA beads were incubated with the supernatant containing His-tagged fusion Tpm and mixed on an orbital shaker at 4°C, 1 h. The beads were loaded on a plastic column and washed extensively with low salt and high salt binding buffer and eluted in elution buffer (50 mM Tris-HCl pH 7.5, 300 mM NaCl, 250 mM imidazole, 1 mM DTT). The wash and eluted fractions were analyzed by SDS-PAGE. The elutes were dialyzed in dialysis buffer (10 mM HEPES pH 8.0, 20 mM NaCl, 1 mM DTT), overnight at 4°C. The supernatant was concentrated and purified by gel filtration against gel filtration buffer with high salt (10 mM HEPES pH 8.0, 500 mM NaCl, 1 mM DTT). The peak fractions were analyzed by SDS-PAGE, pooled together and concentrated. The protein concentration was measured by fluorimetry, and the aliquots were flash-frozen and stored at −80°C.

Co-sedimentation assays

Actin co-sedimentation assays were performed as previously reported with few modifications.[8] Non-muscle actin (β/γ-actin from human platelets) was procured from Cytoskeleton Inc. and was resuspended in distilled water and stored at −80°C as per the manufacturer's instructions. For co-sedimentation assays using cofilin-1, different amounts of either β/γ-actin or β/γ-actin and non-tagged Tpm1.6 or Tpm3.2 were mixed in presence of G-buffer (5 mM HEPES pH 6.6, 0.2 mM $CaCl_2$, 0.2 mM DTT and 0.2 mM ATP). To saturate Tpm binding site on non-muscle actin filaments, actin and Tpm1.6 or Tpm3.2 were mixed in 4.7:1 and 4:1 ratios, respectively. Actin:Tpm were pre-polymerized by addition of F-buffer containing 20 mM HEPES pH 6.6, 100 mM KCl, 5 mM $MgCl_2$, 0.2 mM EGTA, 10 mM DTT and 2 mM ATP final concentration at room temperature for 30 min. One μM of cofilin-1 was added to the polymerized actin:Tpm complex and was incubated at room temperature for 30 min. Actin:Tpm:cofilin-1 protein complex was sedimented by centrifugation at 57,000 rpm for 60 min at 10°C (TLA100 rotor, Beckman Optima MAX Ultracentrifuge). Supernatant and pellet fractions were separated, and samples were prepared for SDS-PAGE analysis by cooking in Laemmli Buffer at 100°C for 5 min. Supernatant and pellets were run on 4–20% gradient SDS-PAGE gels in equal proportions (Mini-PROTEAN TGX Precast Gels, Bio-Rad Laboratories Inc.). The gels were stained with Coomassie Blue staining solution (QC Colloidal Coomassie stain, Biorad Laboratories, Inc.). The intensities of cofilin-1 protein bands was quantified with Fiji ImageJ (version 1.53t) program, analyzed using Microsoft Excel worksheet (version 2016) and plotted as the amount of cofilin-1 protein bound (μM) to actin:Tpm1.6/actin:Tpm3.2.

Pyrene-actin quenching assay

The assay was performed using a Cary Eclipse fluorescence spectrophotometer (Agilent Technologies). Human non-muscle β/γ-actin (95%) and rabbit skeletal muscle pyrene-labeled actin (5%) (both procured from Cytoskeleton, Inc.) was polymerized at room temperature for 30 min in polymerization buffer containing 20 mM HEPES pH 6.6, 100 mM KCl, 5 mM $MgCl_2$, 0.2 mM EGTA, 10 mM DTT and 2 mM ATP. The filaments were further incubated with tropomyosins for 30 min with the following protein molar ratios: 4.7:1 (actin:Tpm1.6) and 4:1 (actin:Tpm3.2) to saturate the actin filaments with Tpms. The reaction was initiated by mixing 2 μM actin (or Tpm-saturated actin) with 2 μM Cofilin-1 (final concentrations), and the fluorescence was recorded for 30 min at room temperature with an excitation and emission wavelengths of 365 nm and 407 nm, respectively.

In-vitro TIRF microscopy

The TIRF chamber was pre-treated with 1.5% BSA for 1 h in a humidified chamber. β/γ-actin, sfGFP-fused Tpm1.6, Tpm3.2 and mCherry-fused Cofilin-1 were diluted in G-buffer containing 5 mM HEPES pH 7.4, 0.2 mM $CaCl_2$, 0.2 mM DTT and 0.2 mM ATP. For polymerization 0.8 μM β/γ-actin was mixed with 1.2 μM sfGFP-Tpm1.6 and 2.4 μM sfGFP-Tpm3.2 in F-buffer (10 mM HEPES pH 7.0, 50 mM Na-acetate, 3 mM $MgCl_2$, 1 mM DTT and 0.2 mM ATP) and incubated at room temperature for 30 min. 1.2 μM of mCherry-cofilin-1 was added to the reaction, followed by 1% methylcellulose final concentration. The reaction was mixed and injected into the BSA pre-treated TIRF chamber. The imaging was started immediately without any delay. TIRF imaging was performed using ONI Nanoimager equipped with 100× Apo TIRF 1.49 NA oil objective, 1000-mW 561-nm and 1000-mW 640-nm lasers, sCmos camera and NimOS software. The time-lapse images were captured for 30 min with 10-s intervals using 3% green and red laser power at 100 fps speed. The time lapse images were analyzed by Fiji ImageJ software. Only single actin:Tpm filaments were measured during the analysis. The growth of cofilin-1 segments in 30 min was analyzed by measuring the length of cofilin-1 segments at the first and the last frame of imaging and subtracting the length obtained at the first frame from the last one. Thus, the rate of cofilin-1 extension on Tpm1.6 and Tpm3.2 decorated actin filaments was obtained by dividing the cofilin-1 segments by imaging time (30 min).

Cryo-EM sample preparation, data collection and image processing

To dissolve the oligomers that form during the storage, 50 μM β/γ-actin was mixed in G-buffer (5 mM HEPES pH 7.4, 0.2 mM $CaCl_2$, 0.2 mM DTT, 0.2 mM ATP), and incubated at room temperature for at least 30 min. To ensure complete saturation of actin filaments with Tpm, a 1:1.5 ratio of β/γ-actin:Tpm1.6 and Tpm3.2 was used for the sample preparation. β/γ-actin (12.5 μM) was mixed to F-buffer (10 mM HEPES pH 7.0, 50 mM Na-acetate, 3 mM $MgCl_2$, 1 mM DTT and 0.2 mM ATP) and incubated at room temperature

for 30 min to allow the formation of actin filaments. Either Tpm1.6 (9 μM) or Tpm3.2 (9 μM) was added, mixed gently, and incubated further for 1 h at room temperature. The actin:Tpm complex was pelleted by centrifugation at 59,000 rpm for 1 h at 10°C (TLA100 rotor, Beckman Optima MAX Ultracentrifuge). The supernatant was discarded and fresh F-buffer containing 0.02% NaN_3 was added to the pellet before incubating it overnight for the pellet to solubilize.

A 3-μL aliquot of the actin-Tpm sample was applied onto a glow-discharged holey carbon copper grid (Quantifoil R1.2/1.3) and allowed to settle for 15 s. The grids were prepared using a vitrification apparatus (Vitrobot, Thermo Fisher Scientific) operated at a relative humidity of 95% and at 6°C. Grids were blotted for 5 s with filter paper prior to plunging into liquid ethane. The grids were stored in liquid nitrogen for subsequent screening and imaging.

Data were acquired using a transmission electron microscope (Talos Arctica, Thermo Fisher Scientific) equipped with Falcon III direct electron detector (Thermo Fisher Scientific). Movies of 45 frames were collected with a total electron exposure of 45 $e^-/Å^2$, with a defocus ranging from 1 to 3 μm. A total of 1,758 movies were recorded for Tpm1.6 and 1,273 movies for Tpm3.2 complex. The movies were then imported to RELION for data processing. The movies were aligned and summed using MotionCor2.[39] CTF was estimated using CTFFIND4.[40] Filaments were manually picked to generate a template for automated picking using 2D classification in RELION.[48] Class averages showing Tpm-decorated filaments were used as templates and filaments were picked automatically using a helical rise of 27.5 Å and a width of 100 Å. Overlapping filament segments were extracted in 400 × 400-pixel boxes and subjected to reference-free 2D classification. Segments corresponding to classes representing bare actin were discarded and the remaining segments were subjected to two rounds of 2D classification. This resulted in 118,164 segments for Tpm1.6 and 100,804 segments for Tpm3.2. An ab initio model was generated for both datasets in RELION. Using this model as a reference, the filament segments were subjected to 3D classification applying helical symmetry. Particles corresponding to 3D class averages displaying Tpm decoration were selected. This resulted in 79,298 segments for Tpm1.6 and 81,431 segments for Tpm3.2. The segments were subjected to 3D reconstruction, using one of the 3D class averages as a reference. Helical symmetry was used during refinement and was allowed to explore the range from −161 to −170 degrees of rotation and a rise from 22 to 30 Å. After particle polishing, CTF refinement, and postprocessing, the final resolution was 3.9 Å for Tpm1.6 and 4.5Å for Tpm3.2 complex, as estimated by Fourier shell correlation (FSC = 0.143). For visualizing the entire length of the actin filament corresponding to Tpms, the map was averaged in real space in a 512 × 512-pixel box by applying helical symmetry in RELION.

Atomic model building and molecular modeling

A comparative model was created for β-actin in SWISS-MODEL[41] using a fiber actin structure (PDB:5JLF) as a template. The resulting structure was fitted into the actin:Tpm cryo-EM density maps as a rigid body using UCSF ChimeraX.[45] The structure was manually adjusted in Coot[42] and in ISOLDE.[43] Symmetry copies (8 chains in total) were generated in ChimeraX by rigid body fitting. A polyalanine model (135 residues, from PDB:3J8A) of Tpm was fitted into the density maps filtered to 7 Å resolution as a rigid body in ChimeraX and refined in ISOLDE in the same density maps using secondary structure restraints. The Tpm models were combined with their respective actin models and the combined models were refined in real space in Phenix[44] against the unfiltered maps, using the parameters created in ISOLDE with command *isolde write phenixRsrInput* with added non-crystallographic symmetry constraints. Structures were validated using Phenix and MolProbity.[49] Figures were made using ChimeraX.

Modeling of the actin:Tpm interfaces was carried out using a combination of AlphaFold structure prediction[50] and Rosetta all-atom refinement.[51,46] For each actin filament, the model was first refined symmetrically into the corresponding cryo-EM density map. These refined actin filament models were then used in the subsequent modeling of Tpms. To identify the contacts between the Tpm and actin interface, the following procedure was performed on both Tpm1.6 and Tpm3.2:

1. Prediction of the Tpm coiled-coil by AlphaFold: A model of the coiled-coil alone was predicted by AlphaFold, using Tpm monomer multiple sequence alignments with a depth of over 2000 sequences. Five models from AlphaFold were minimized in Rosetta using the *Relax* protocol[52] and the lowest-scoring model was chosen. For both sequences, the final model had at least 85% residues with a confidence estimate (pLDDT) greater than 70. Predicted alignment error (PAE) was less than 5 Å for at least 60% of contacts made across the interface of the coiled-coil.
2. Identification of favorable actin–Tpm interfaces: We first identified favorable interactions of actin and Tpm by modeling the energetics of a small piece of Tpm (approximately 45 residues from each Tpm chain) interacting with a single actin monomer. We considered all sequence registrations onto this helix that maintained the predicted coiled-coil interface, by first shifting the helices "up" by one turn (equivalent to a 3.5-residue shift), and then by rethreading the model offset by 7 residues (equivalent to a shift of one heptad repeat). Each model was refined with Rosetta's *Relax* function.
3. Determination of the full-length actin–Tpm interface: We translated the full-length Tpm model in relation to the actin filament in steps corresponding to one helical turn (approximately 5.5 Å) and refined the resulting model. Refinement involved a two-step procedure. Since the predicted Tpm models showed different curvature than was indicated by the density, we first refined Tpm in isolation (with Rosetta's *Relax*) using fit-to-density as well as constraints from the interfaces determined in step 2. Next, we refined the full actin:Tpm complex, using the fit-to-density function without any other constraints (again using *Relax*). In this step, only actin residues within 8 Å of Tpm were permitted to move. For this latter step, five independent trajectories were run. For each position, the interface energies were calculated using the *ddG* application in Rosetta (Figure S5).

4. Final refinement of full actin:Tpm complex: The model from step 3 with the lowest interface energy was refined using Rosetta's *LocalRelax* protocol.[46] Twenty models were generated, and the lowest energy model was selected, using Rosetta's force field augmented with the "fit to density" score term.

QUANTIFICATION AND STATISTICAL ANALYSIS

All the data from the co-sedimentation assay, pyrene-actin quenching assay, and *in-vitro* TIRF microscopy were documented and analyzed using Microsoft Excel worksheet (version 2016). The final graphical representations were prepared using GraphPad Prism 7.03 software. An unpaired t test with Welch's correction was performed to determine the statistical significance of cofilin-1 decoration of actin filaments in the *in-vitro* TIRF experiment. The significance between actin:Tpm1.6 and actin:Tpm3.2 filaments binding to cofilin-1 in co-sedimentation assay was determined using two-tailed unpaired t test with 95% confidence intervals. All biochemical experiments were repeated independently at least three times.